Title

An oceanic heat transport pathway to the Amundsen Sea Embayment

Journal

Journal of Geophysical Research - Oceans, 121(5)

ISSN

2169-9275

Authors

Rodriguez, Angelica R
Mazloff, Matthew R
Gille, Sarah T

Publication Date

2016-05-01

DOI

10.1002/2015jc011402

Peer reviewed

AGU PUBLICATIONS

JGR

Journal of Geophysical Research: Oceans

RESEARCH ARTICLE

10.1002/2015JC011402

Key Points:
- The divergence of heat advection leads to change in oceanic heat content.
- Cross-shelf heat input dominates the ASE heat content at depth.
- Vorticity input from the local wind-stress curl sustains cross-shelf transport.

Correspondence to:
A. R. Rodriguez,
arodrigu@ucsd.edu

Citation:
Rodriguez, A. R., M. R. Mazloff, and S. T. Gille (2016), An oceanic heat transport pathway to the Amundsen Sea Embayment, *J. Geophys. Res. Oceans*, *121*, doi:10.1002/2015JC011402.

Received 18 NOV 2015
Accepted 18 MAR 2016
Accepted article online 23 MAR 2016

An oceanic heat transport pathway to the Amundsen Sea Embayment

Angelica R. Rodriguez[1], Matthew R. Mazloff[1], and Sarah T. Gille[1]

[1]Scripps Institution of Oceanography, University of California San Diego, La Jolla, California, USA

Abstract The Amundsen Sea Embayment (ASE) on the West Antarctic coastline has been identified as a region of accelerated glacial melting. A Southern Ocean State Estimate (SOSE) is analyzed over the 2005–2010 time period in the Amundsen Sea region. The SOSE oceanic heat budget reveals that the contribution of parameterized small-scale mixing to the heat content of the ASE waters is small compared to advection and local air-sea heat flux, both of which contribute significantly to the heat content of the ASE waters. Above the permanent pycnocline, the local air-sea flux dominates the heat budget and is controlled by seasonal changes in sea ice coverage. Overall, between 2005 and 2010, the model shows a net heating in the surface above the pycnocline within the ASE. Sea water below the permanent pycnocline is isolated from the influence of air-sea heat fluxes, and thus, the divergence of heat advection is the major contributor to increased oceanic heat content of these waters. Oceanic transport of mass and heat into the ASE is dominated by the cross-shelf input and is primarily geostrophic below the permanent pycnocline. Diagnosis of the time-mean SOSE vorticity budget along the continental shelf slope indicates that the cross-shelf transport is sustained by vorticity input from the localized wind-stress curl over the shelf break.

1. Introduction

The West Antarctic Ice Sheet (WAIS) contains 3.8 million km^3 of ice [*Oppenheimer*, 1998] and has the potential to cause global eustatic sea level rise of more than 3 m [*Bamber et al*., 2009]. Thus, the stability of WAIS has been the focus of much current research [*Joughin and Alley*, 2011; *Joughin et al*., 2014; *Rignot et al*., 2014]. Satellite observations have shown that the most significant ice mass loss occurs along the Amundsen Sea coastline where several outlet glaciers drain into the embayment [*Rignot et al*., 2008, 2013; *Pritchard et al*., 2012]. Ice flow in this region has increased by 77% since the 1970s [*Mouginot et al*., 2014]. Thinning of the floating ice-shelves and glacial grounding line retreat have been attributed to basal melting forced by heat input from inflowing Circumpolar Deep Water (CDW) [*Payne et al*., 2004; *Walker et al*., 2007; *Wåhlin et al*., 2010]. CDW in the Amundsen Sea Embayment (ASE) is typically 3–4°C warmer than the in situ freezing point and can be found as far south as the grounding zone of the Pine Island Glacier (PIG) [*Jenkins et al*., 2010; *Jacobs et al*., 2011]. On monthly timescales, basal melt is thought to be driven largely by processes outside the subice-shelf cavity [*Schodlok et al*., 2012; *Heimbach and Losch*, 2012]. Hence, knowledge of the ocean state at the continental shelf slope is crucial to modeling studies of subice-shelf processes.

An understanding of the delivery mechanisms of CDW to the ASE is essential to predicting further influence of ocean forcing on the outlet glaciers of the ASE. A modeling study by *Thoma et al*. [2008] linked cross-continental-shelf CDW transport variability to zonal wind variability along the continental shelf edge due to migration of the Amundsen Sea Low. Building upon these results, *Steig et al*. [2012] proposed that tropical Pacific warming brought about the modern period of PIG retreat through a shift in the ASE zonal wind regime.

This study aims to investigate the large-scale pathways of CDW delivery to the ASE. Our primary tool is a Southern Ocean State Estimate (SOSE) [*Mazloff et al*., 2010], which provides a realistic model of the Southern Ocean dynamics and physical properties, as well as atmospheric forcing, through assimilation of all available observations. It uses the OCean Comprehensible Atlas (OCCA) global state estimate [*Forget*, 2010] to constrain the initial and northern boundary conditions and the European Centre for Medium-Range Weather Forecasts (ECMWF) Reanalysis (ERA)-Interim (http://www.ecmwf.int/) to constrain the meteorological boundary conditions at the ocean-atmosphere interface. Because the SOSE solution includes the entire Southern

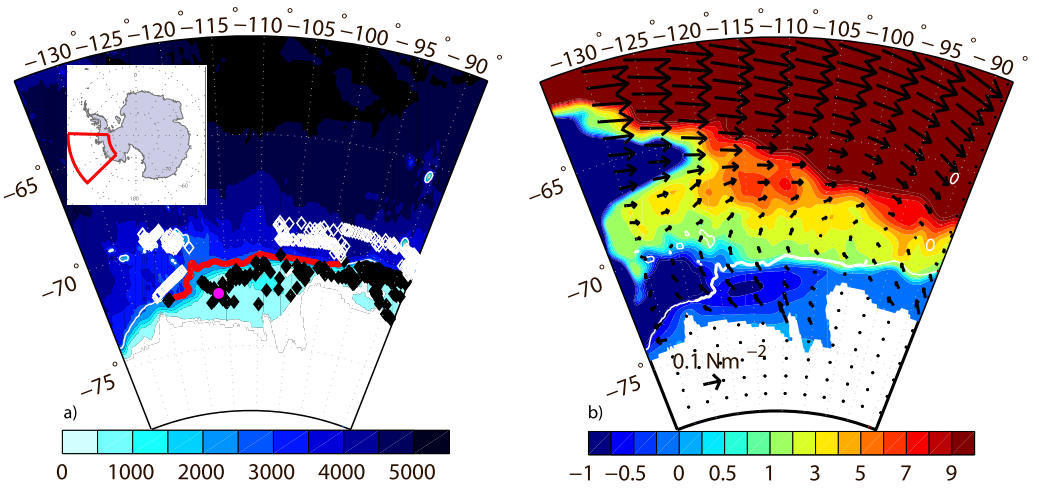

Figure 1. (a) The Amundsen Sea bathymetry (m) with 2005–2010 CTD, Argo, and SEaOS observation locations. White diamonds indicate observations north of the shelf break, while black diamonds indicate shallower observations. The magenta circle indicates the location of the mooring data presented in Figure 3. The red 2600 m depth contour indicates the perimeter of the ASE. For the purposes of this analysis, lateral boundaries of the ASE are at 124.25°W and 98.42°W. b). The 2005–2010 time-mean streamfunction (Sv) with 2005–2010 time-mean wind-stress vectors. For reference, the 2600 m bathymetric contour of the continental shelf is also plotted in white to indicate the location of the shelf break relative to the time-mean currents.

Ocean, it provides a perspective on the delivery of warm water to the ASE that is physically consistent with the Southern Ocean as a whole. This contrasts with previous regional modeling studies [e.g., *Thoma et al*., 2008; *Heimbach and Losch*, 2012], which may be more sensitive to boundary and initial conditions. Being large-scale, however, does come at the expense of resolution, and we discuss these limitations in section 2.

The analysis tool, SOSE, is further discussed in section 2. In section 3, we compare SOSE to observations in the Amundsen Sea near the continental shelf and within the ASE. We diagnose the heat budget of the ASE waters along the continental shelf slope in section 4 with the goal of identifying the factors that most strongly dictate changes in the heat content of these waters. In section 5, we quantify mass and heat transports into and out of the embayment, and find that the oceanic transport of heat to the ASE is dominated by a time-mean geostrophic flow across the continental shelf slope. This transport is attributed to forcing by a strong local wind-stress curl that drives waters poleward onto the ASE continental shelf in section 6, followed by a summary and discussion in section 7.

2. The Southern Ocean State Estimate

SOSE, the primary tool in this study, is an eddy-permitting general circulation model constrained to observations. It uses the MITgcm configured with 1/6° horizontal resolution, 42 vertical levels of varying thickness, and a time step of 900 seconds [*Mazloff et al*., 2010]. SOSE employs a sea ice model based on the work of *Semtner* [1976] for the thermodynamics [*Fenty and Heimbach*, 2013] and on the work of *Hibler and Bryan* [1987] for the dynamics [*Zhang and Hibler*, 1997; *Losch et al*., 2010]. SOSE observational constraints include Argo floats, conductivity-temperature-depth (CTD) casts, Southern Elephant Seals as Oceanographic Samplers (SEaOS) instrument mounted seal profiles, expendable bathythermograph (XBT) profiles, inverted echo sounders (IES), radiometric sea surface temperature measurements, altimetric observations, and sea ice cover observations.

For this study, we use a SOSE solution for the years 2005–2010. The output, denoted iteration 100, is available from sose.ucsd.edu. We define the ASE as the region extending from the Antarctic coast to the continental shelf slope defined by an along-shelf coordinate that follows the 2600 m depth contour of the SOSE bathymetry between 124.25°W and 98.42°W, indicated by the red contour in Figure 1a. In situ observations in the ASE region, which were minimal from 2005 to 2007, but prevalent from 2008 to 2010, are indicated in Figure 1.

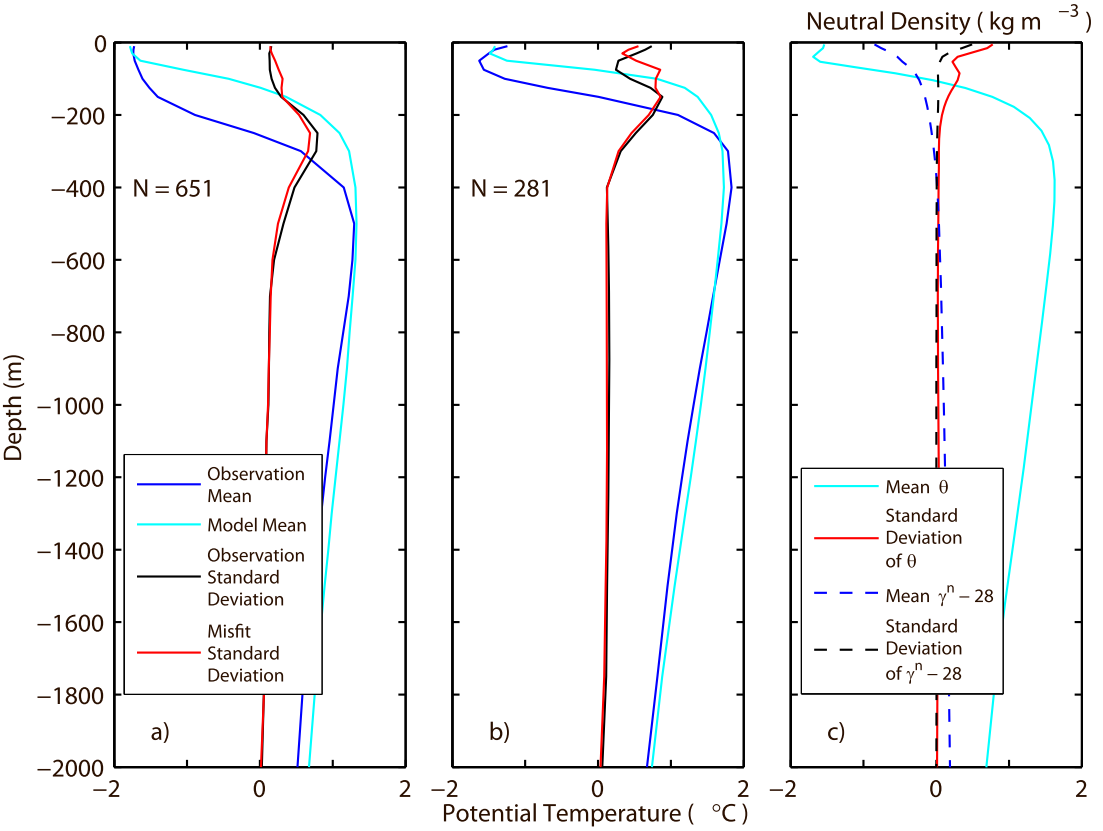

Figure 2. Mean potential temperature profiles (blue lines) of the 2005–2010 observations at (a) shallow locations (filled black diamonds in Figure 1a) and (b) deep locations (unfilled white diamonds in Figure 1a). N is the number of observed profiles for each regime. Also shown are the standard deviations of the mean profiles (black lines), mean potential temperature profiles (cyan lines) of the model equivalents to the observations, and standard deviation of the model misfit $(\text{model}_i - \text{observation}_i)$ (red lines). (c) Time-mean model temperatures (cyan line) and neutral density relative to 28 kg m^{-3} (blue-dashed line) averaged along the 2600 m bathymetric contour that defines the northern edge of the ASE and temporal standard deviations (red and black-dashed lines, respectively).

While SOSE is eddy-resolving equatorward of the ACC, the horizontal resolution is too coarse to resolve mesoscale structures at the latitude of the Antarctic continental shelf slope, where the first baroclinic mode Rossby radius decreases to 5 km [*Venaille et al.*, 2011]. However, the modeled heat transport into the ASE at the continental shelf slope is necessarily physically consistent with the ACC to the north, which is constrained to observations. Thus, the analysis carried out here is able to reveal the large-scale (greater than ∼75 km) pathways of heat transport to the ASE, as well as the dynamics governing these pathways on time-scales greater than 2 days. Dynamics occurring at smaller scales, including eddies and tides, also play a significant role in facilitating cross-shelf heat exchange in several different regions along the Antarctic continental shelf [*Robertson*, 2013; *Martinson and McKee*, 2012; *Nøst et al.*, 2011; *Thompson et al.*, 2014; *Stewart and Thompson*, 2015]. The roles of these processes, and their interaction with the large-scale flow over sloping topography are beyond the scope of the present study.

3. Model Comparison to Observations

To determine if SOSE is consistent with the observed ASE properties, we use CTD, Argo, and SEaOS profiles (depicted as diamonds in Figure 1a) taken between 2005 and 2010. All seasons are represented in the available data sets, with the majority of wintertime observations from the SEaOS program. The last three years of the solution contain significantly more data than the first three years due to an increase in Argo profiling floats in the region. Observations taken south of the 2600 m isobath are indicated by filled black diamonds, while those just north of the ASE study domain are white and unfilled. Figures 2a and 2b depict the mean (blue) and standard deviation (black) of the observed potential temperature on and off of the shelf, respectively. Observed potential temperatures on the shelf exhibit a deeper mixed layer with a more gradual

thermocline than those off of the shelf. Both regions show strongest variability in the thermocline. The differences in structure between the model and observations are found in all seasons, with the greatest variability found above the 225 m permanent pycnocline.

The mean of the SOSE equivalent to the 2005–2010 observations of potential temperature is also plotted (cyan), along with the root-mean-squared difference of the model-observation misfit (red). In both regions, SOSE exhibits a mixed layer that is too thin, leading to a modeled thermocline that is shallower than observed. However, all observed water masses are exhibited in SOSE. Thus, though SOSE's mixed layer is biased shallow, it has the same structure and temperature as seen in observations. We are primarily interested in the movement of deep warm water across the continental shelf slope, as this is thought to be the primary source of heat driving increased basal melt rates of ASE outlet glaciers. Although an elevated thermocline indicates that the warm water reaches too high in the water column in SOSE, the modeled ocean temperature does have the same structure and magnitude as observed.

In SOSE, the potential temperature profile, referenced to 0 dbar, averaged along the continental shelf slope is near freezing (~ -1.7°C) at the surface and warms quickly with depth to peak at $\sim$1.6°C at 439 m depth (Figure 2c). The profile then decreases with depth approaching 0°C at the bottom. These water temperatures have significant atmospheric-driven temporal variability in the upper 225 m but are relatively constant below that depth, as indicated by the temporal standard deviation (Figure 2c). Therefore, when discussing calculations involving model temperature, we separate the analysis into surface and subsurface boxes, separated in depth at 225 m.

The 2005–2010 time-averaged SOSE neutral density along 225 m depth differs between the west end of the shelf and the east end by only 0.014 kg m^{-3}, with slightly warmer, lighter water to the east. Density classes below 225 m differ even less in the horizontal. Temporal variability below 225 m is minimal as well, as indicated by the black-dashed line in Figure 2c. *Whitworth et al*. [1998] define CDW to be the water mass with neutral density between 28.00 and 28.27 kg m^{-3}. Several studies suggest that this water mass is the most significant to thermal forcing of ASE marine-terminating glaciers. We find this water mass along the continental shelf slope in SOSE, indicated by the mean neutral density profile (blue-dashed line). This curve is shifted by the upper limit of CDW in the ASE [*Whitworth et al*., 1998] ($\gamma^n - 28$ kg m^{-3}), and thus, negative values found in the upper water column indicate water masses lighter than CDW. The variability of water mass properties above and below 225 m depth is the basis for vertical separation of the heat budget and transport analysis described in sections 4 and 5.

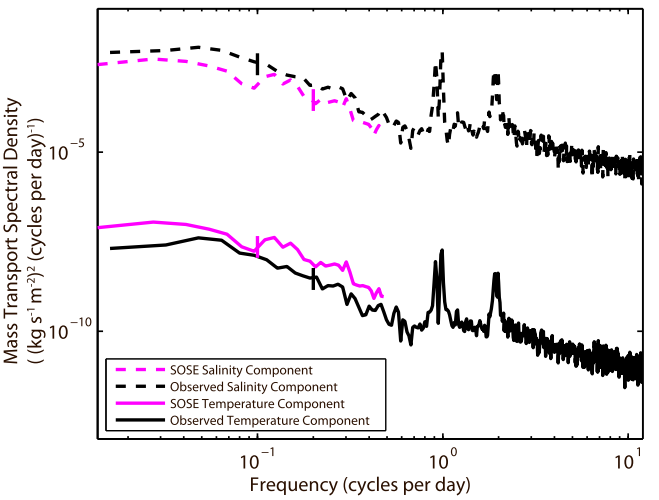

Figure 3. Comparison of salinity and temperature data observed from a mooring located at 72.46°S, 116.35°W [*Wåhlin et al*., 2013] (black lines) to the SOSE equivalents (magenta lines). The figure shows spectral density of the salinity components (dashed lines) and temperature components (solid lines) of mass transports ((kg s^{-1} m^{-2})^2 (cycle per day)$^{-1}$) in the direction of the principal axis of velocity at 506 m depth. Vertical bars correspond to the 95% confidence interval that the estimated spectra is the true spectra.

The model velocity field from the year 2010 is compared to mooring observations located at 72.46°S, 116.35°W (Figure 1a). Figure 3 shows spectral estimates of the salt and temperature components of mass transport at 506 m depth, with transport defined in the direction of the principal component of horizontal velocity at this depth. Both the observed and modeled transports are in the direction of maximum variance. The salinity and temperature transports, *uS* and *uT*, are scaled to units of mass transport using $\partial\rho/\partial T|_S = -0.11$ kg m^{-3}°C^{-1} and $\partial\rho/\partial S|_T = 0.80$ kg m^{-3} PSU^{-1}. Daily averaged velocity, salinity, and temperature in SOSE resolves spectral density at frequencies of 0.5 cycles per day and lower, while higher frequency variability is not resolved. At the resolved

frequencies, the model is consistent with observations. The variance in the salinity component of modeled mass transport, 2.4 $\times$ 10^{-2} (kg s^{-1} m^{-2})^2, is five orders of magnitude higher than the variance of the temperature component of mass transport, 6.9 $\times$ 10^{-7} (kg s^{-1} m^{-2})^2, indicating that temperature at this depth is relatively steady during 2010 at this location. For the remainder of the analysis presented here, we focus on dynamics governing the heat budget on monthly time-scales and longer at spatial scales of 75 km and larger.

While SOSE captures the structure and magnitude of observed temperature in the ASE, as well as the energetics of the circulation, it does not employ an ice-shelf model, and thus, while the oceanic heat budget is closed, it does not involve ice/ocean interactions that occur along the ice-sheet margin. In addition to modifying the continental shelf circulation that we do not adequately resolve, this interaction would decrease the total temperature tendency and input freshwater to the ocean system. Though ice-shelf and ocean interaction changes water mass properties and is important to quantify, its role in governing the transport of heat across the continental shelf slope is probably small and left for further investigation.

4. The Vertically Separated Heat Budget

In order to understand the processes most affecting the heat content of the ASE shelf waters during the years 2005 to 2010, we compute the time-varying potential temperature, referenced to 0 dbar,

$$\underbrace{\theta_t}_{\text{tendency}} = \underbrace{-u\theta_x - v\theta_y - w\theta_z}_{\text{advection}} + \underbrace{\nabla\cdot\kappa\nabla\theta + \nabla^2\cdot\kappa_4\nabla^2\theta + \mathcal{D}_{KPP} + \mathcal{D}_i}_{\text{diffusion}} + \underbrace{\mathcal{F}_{\text{atm}} + \mathcal{F}_{\text{ice}}}_{\text{forcing}} \quad (1)$$

$$= \quad -\mathbf{u}\cdot\nabla\theta \quad + \quad \mathcal{D} \quad + \quad \mathcal{F},$$

where $\mathbf{u}=u\hat{\mathbf{i}}+v\hat{\mathbf{j}}+w\hat{\mathbf{k}}$ is the velocity vector, κ and κ_4 are the harmonic and biharmonic diffusion coefficients, $\mathcal{D}_{KPP}$ represents the parameterization of mixed-layer turbulence by the K-Profile Parameterization (KPP) [*Large et al.*, 1994], $\mathcal{D}_i$ represents implicit diffusion in the model, and $\mathcal{F}_{\text{ice}}$ and $\mathcal{F}_{\text{atm}}$ represent ocean exchanges with sea ice and the atmosphere. Here the model assumes incompressible flow ($\nabla\cdot\mathbf{u}=0$). SOSE solves for each individual term in 1. We group the divergence of the advective terms into one *advection* term ($\mathbf{u}\cdot\nabla\theta$); the harmonic, biharmonic, parameterized, and implicit diffusion terms into a *diffusion* term ($\mathcal{D}$); and fluxes from both sea ice and the atmosphere into one *forcing* term ($\mathcal{F}$). Since we separate surface and subsurface waters by depth, not density, the advective term includes adiabatic vertical advection between the two boxes, discussed in greater detail in subsection 5b on heat transports. Profiles of $\mathcal{D}_{KPP}$ diffusion coefficient (not shown) indicate strong mixing in the top 50 m of the water column and rapid decay to a constant value of 10^{-5} m^2 s^{-1} below 150 m depth. However, $\mathcal{D}_{KPP}$ has not been validated or tuned for the conditions found on the Amundsen Sea Continental Shelf. The shallow thermocline bias identified in section 2 is likely a result of too shallow parameterized mixing.

We consider three components governing the temperature tendency: advection by ocean currents, parameterized turbulent mixing, and external forcing. Over the 6 years analyzed, the net mass divergence in the modeled ASE is negligible, so the ASE heat budget is well approximated by integrating equation (1) over the volume of the ASE and multiplying by the specific heat capacity, $C_v = 3985$ J $kg^{-1}{}^{\circ}C^{-1}$, and mean seawater density, $\rho_0 = 1035$ kg m^{-3}. This formulation is consistent with that of *Warren* [1999].

Time series of the surface heat budget terms integrated over the volume of the ASE study domain reveal that at times of low ice concentration atmospheric forcing dominates the budget, with heat input reaching a magnitude of 46.3 TW (Figure 4b). Heat input from advection has a maximum of 17.2 TW and governs the heat content when sea ice is insulating the ocean from the atmosphere. The diffusive heat flux is an order of magnitude smaller than the tendency throughout 2005–2010. Temporal integration of the surface heat budget terms via a cumulative sum in time confirms that the temperature tendency primarily tracks atmospheric forcing throughout 2005–2010 (Figure 4d). Strong atmospheric cooling in the fall combined with relatively weak cooling in winter and spring dominate significant atmospheric heating in austral summer, resulting in a net heat flux from the ASE to the atmosphere. Oceanic heat transport compensates the atmospheric cooling, averaging 1.29 TW and thus contributing 24.5$\times$$10^{19}$ J of advective heating between 2005 and 2010. The combined effect of ocean heat transport and atmospheric and sea ice exchange is a net increase in heat content of the ASE surface waters of 8.24$\times$$10^{19}$ J, equivalent to a warming of 0.34°C, over the 6 year simulation.

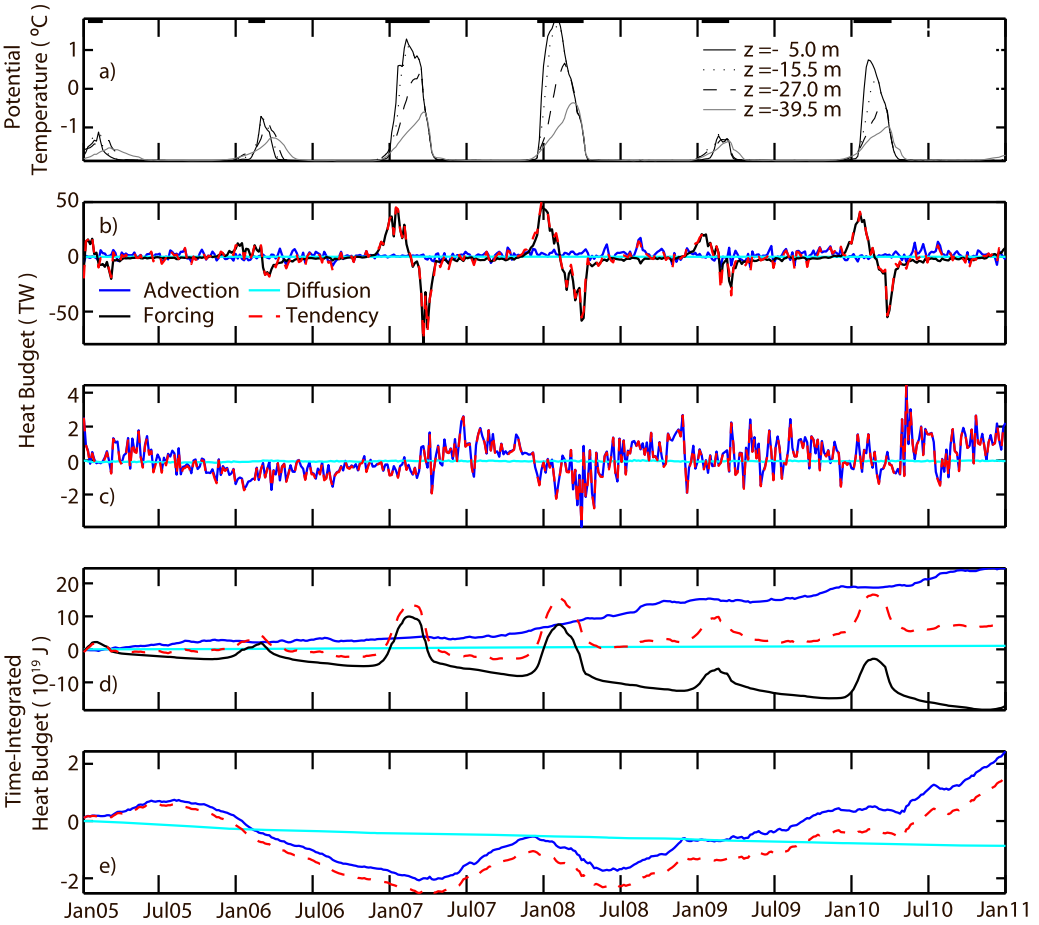

Figure 4. (a) Potential temperature averaged along the 2600 m isobath at four depths near the ocean surface with bold black lines placed at the maximum temperature value depicting the length of time that sea ice covers less than 65% of the ASE. (b) Heat budget above 225 m depth (surface). (c) Heat budget below 225 m depth (bottom). The blue lines in Figure 4b and c are the same as the blue lines in Figures 5a and 5b, respectively. (d) Time-integrated surface heat budget. (e) Time-integrated bottom box heat budget. For Figures 4b–4e, the red-dashed line is the total tendency, the black line is the atmospheric forcing, the blue line is advection, and the cyan line is diffusion.

Below 225 m depth advection and diffusion govern the heat budget, since atmospheric fluxes do not directly reach these depths. Advective heat transport dominates over the diffusive heat fluxes and therefore dictates the tendency (Figure 4c). The time-integrated subsurface heat budget (Figure 4e) shows a cooling trend between July 2005 and April 2007 with a subsequent increase and decrease over the next year, leading to a consistent warming trend between July 2008 and December 2010. The time-integrated tendency yields a total change in heat content of 1.57×10^{19} J, equivalent to a volume average change in θ of 0.02°C, in the waters in the ASE below 225 m depth over the 6 year simulation, with much of this heating occurring between 2008 and 2010.

5. Transport Calculations

5.1. Vertically Separated Mass Transports

Strong currents, which are associated with the Southern Antarctic Circumpolar Current Front (SACCF), are found north of the continental shelf (Figure 1b). The southward meander of the Antarctic Circumpolar Current (ACC) in this region can be explained, in part, by wind-stress curl, which is consistent with the local Sverdrup balance. The 2005–2010 time-averaged winds over the Amundsen Sea are westerly and almost completely zonal north of 65°S. Over the ASE the mean winds are katabatic, blowing from the continent in the northward direction. The mean winds between the ASE and 65°S transition from northward to eastward, and thus exhibit a significant curl. A measure of how the ASE circulation couples with the Southern Ocean to the north can be evaluated by quantifying the total mass transport across each boundary of the study

Table 1. Mass Transports

Transports (Sv)	Along-Shelf From the West at 124.25°W	Along-Shelf From the East at 98.42°W	Cross-Shelf
2005	-0.05 ± 2.22	-1.27 ± 0.93	1.32 ± 0.64
2006	0.72 ± 0.72	-1.36 ± 0.69	0.64 ± 0.51
2007	-0.65 ± 1.08	-0.75 ± 1.00	1.40 ± 0.81
2008	-0.71 ± 1.30	-0.33 ± 1.22	1.04 ± 0.58
2009	-1.02 ± 1.20	-0.25 ± 1.00	1.27 ± 0.65
2010	-1.81 ± 1.13	-0.10 ± 0.94	1.71 ± 0.67
6 year	-0.59 ± 1.36	-0.64 ± 1.10	1.23 ± 0.73

domain (Table 1). The 6 year mean and standard deviation of the transports reveal an on-shelf flow of 1.23 Sv $\pm$ 0.73 Sv, with highly variable compensating outflows at the lateral study domain boundaries. The annual means of the on-shelf flow are low in 2005 and 2006, but significant for the remaining years. The annual means of the along-shelf flow have the same sign over most of the time period, but these transports are so variable that the mean is insignificant.

5.2. Vertically Separated Heat Transports

The ocean currents of the Amundsen Sea carry significant amounts of heat on and off the shelf. The advective term in equation (1) is given by the divergence of potential temperature transport into and out of the ASE. We calculate this transport at each domain boundary by integrating the normal component of $\mathbf{u}\theta$ in the vertical and along the length of the boundary. The sum of temperature transports across each domain boundary is equal to the advective contribution to the temperature tendency and can be expressed in units of heat by multiplying by the C_v and ρ_0.

The heat transport between the upper and lower boxes is taken into account when calculating the net transport, and is shown in Figure 5. By definition, the vertical flux that decreases heat content in one box, increases the heat content of the other box. The 2005–2010 mean vertical advective flux is 0.35 TW from the deeper box to the shallower box. However, this transport is adiabatic and not directly indicative of diapycnal fluxes. While this value is comparable to the net transport in the time-mean, the time-varying vertical transport remains an order of magnitude smaller than the horizontal transports.

Time series of the heat transports within the surface box (Figure 5a) show large temporal variability relative to the mean, particularly in the cross-shelf advective transport (green line) with a maximum net transport of 11.05 TW and a minimum of -8.43 TW. Consequently, the net heat transport divergence (blue line) in the ASE also varies significantly from month to month. Heat transports into the bottom box have lower variance (Figure 5b). With the exception of two short periods in 2007, the cross-shelf heat transport remains positive throughout 2005–2010, with a maximum of 13.81 TW occurring in December 2008. As with the mass transports, heat generally flows out of the ASE at the east and west study domain boundaries, offsetting the cross-shelf input.

Table 2 provides a summary of the annually averaged heat transport across each border of the study domain, as well as the corresponding net advective heat transport divergence. In the surface box, annually averaged total net fluxes remain positive from 2005 through 2010. Mean values indicate that heat is advected in from the west across 124.25°W with an outflow at 98.42°W. However, these fluxes are highly variable with large standard deviations compared to the mean values. This is also the case for the cross-shelf transport with a 6 year mean flux of 0.20 TW and a standard deviation of 2.74 TW. At depth, the heat advection follows the same circulation pattern as the mass transports, into the ASE across the shelf, and out of the bay at both lateral study domain boundaries except in 2005 and 2006, when heat and mass transport are into the domain from the west across 124.25°W. There is significant variation in the along-shelf flow, as indicated by the standard deviations listed in Table 2. The cross-shelf flow, however, maintains a significant positive annual mean, with a 6 year average magnitude of 5.85 TW and standard deviation of 3.35 TW. The dynamics driving cross-shelf advection into the ASE are further examined in the following sections.

5.3. Total Cross-Shelf Heat Transport Decomposition

The main source of heat to the ASE is the divergence of temperature advection in the waters below 225 m. The volume-integrated heat budget is highly variable, but further analysis of the circulation of mass and heat in the

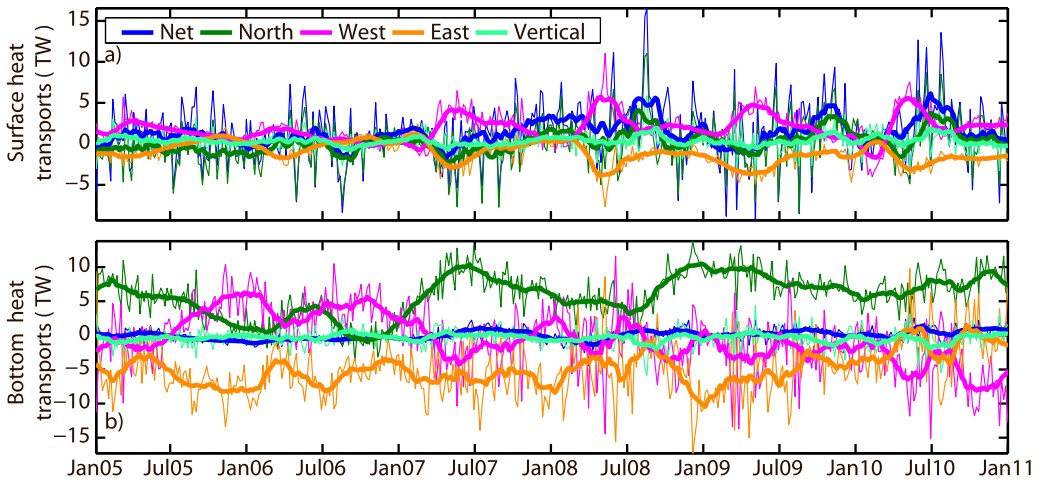

Figure 5. (a) Surface box advective heat transports. (b) Bottom box advective heat transports. The blue line is the net transport, the dark green line is the cross-shelf transport, the orange line is the along-shelf transport from the east across 98.42°W, the magenta line is the along-shelf transport from the west across 124.25°W, and the light green line is the vertical transport between the two boxes. The thick lines are a 1 month moving average for easier visualization.

ASE reveals that the variance is due to the outflow of heat along the shelf at the longitudinal boundaries, while the cross-shelf transports are comparatively steady in time. The cross-shelf transports can be decomposed into geostrophic and ageostrophic components such that $\mathbf{u}^{\perp}=\mathbf{u}_g^{\perp}+\mathbf{u}_a^{\perp}$, where $\mathbf{u}_g=(f\rho)^{-1}(-p_y\hat{\mathbf{i}}+p_x\hat{\mathbf{j}})$ and $\mathbf{u}_g^{\perp}$ is the component of velocity normal to the continental shelf cross section that is in balance with the pressure gradient. The ageostrophic velocity, $\mathbf{u}_a$, includes all motions not in balance with the pressure gradient. Additionally, the total transport can be decomposed into the time-mean and eddy components, such that $\mathbf{u}^{\perp}=\overline{\mathbf{u}^{\perp}}+\mathbf{u}^{\perp\prime}$, where the bar denotes the time-mean and the prime denotes deviations from this mean. The temperature transport then becomes

$$\overline{\mathbf{u}^{\perp}\theta}=\overline{\mathbf{u}_g^{\perp}}\,\overline{\theta}+\overline{\mathbf{u}_g^{\perp\prime}\theta\prime}+\overline{\mathbf{u}_a^{\perp}\theta}. \tag{2}$$

Temperature transports coming into the embayment across the continental shelf slope are dominated by the time-mean geostrophic flow, $\overline{\mathbf{u}_g^{\perp}}\ \overline{\theta}$ (Figure 6). The majority of this transport is a result of the meridional flow across the slope toward the ASE ice-shelves. Unsurprisingly, given the resolution of SOSE, the eddy contribution is small, and ageostrophic motions, such as Ekman transport, are surface intensified. Though the shelf slope is steep enough to act as a strong topographic barrier, there is nonetheless significant time-mean cross-shelf flow.

Table 2. Advective Heat Transports

Upper Box Fluxes (TW)	Along-Shelf From the West at 124.25°W	Along-Shelf From the East at 98.42°W	Cross-Shelf	Total Net Flux
2005	1.54 ± 0.96	−0.38 ± 1.06	−0.79 ± 2.03	0.78 ± 2.85
2006	0.77 ± 0.89	−0.30 ± 0.96	−0.30 ± 2.32	0.32 ± 3.00
2007	1.91 ± 1.91	−0.56 ± 1.57	−0.40 ± 2.40	1.11 ± 2.84
2008	2.42 ± 2.07	−1.37 ± 1.65	1.03 ± 3.07	2.67 ± 3.84
2009	2.28 ± 1.63	−2.18 ± 1.20	0.80 ± 3.17	1.19 ± 4.26
2010	2.11 ± 2.47	−1.61 ± 1.15	0.85 ± 2.74	1.86 ± 3.64
Bottom Box Fluxes (TW)	**Along-Shelf From the West at 124.25°W**	**Along-Shelf From the East at 98.42°W**	**Cross-Shelf**	**Total Net Flux**
2005	1.12 ± 4.12	−5.80 ± 3.49	4.88 ± 2.76	−0.21 ± 0.71
2006	3.84 ± 2.81	−5.64 ± 2.72	1.40 ± 2.31	−0.54 ± 0.46
2007	−0.77 ± 3.66	−−6.19 ± 3.21	7.37 ± 2.70	0.22 ± 0.86
2008	−0.71 ± 4.39	−4.85 ± 4.67	6.06 ± 2.90	−0.10 ± 1.16
2009	−2.06 ± 3.81	−5.56 ± 3.75	8.17 ± 2.00	0.26 ± 0.80
2010	−4.81 ± 4.22	−1.27 ± 4.06	7.13 ± 2.20	0.53 ± 1.06

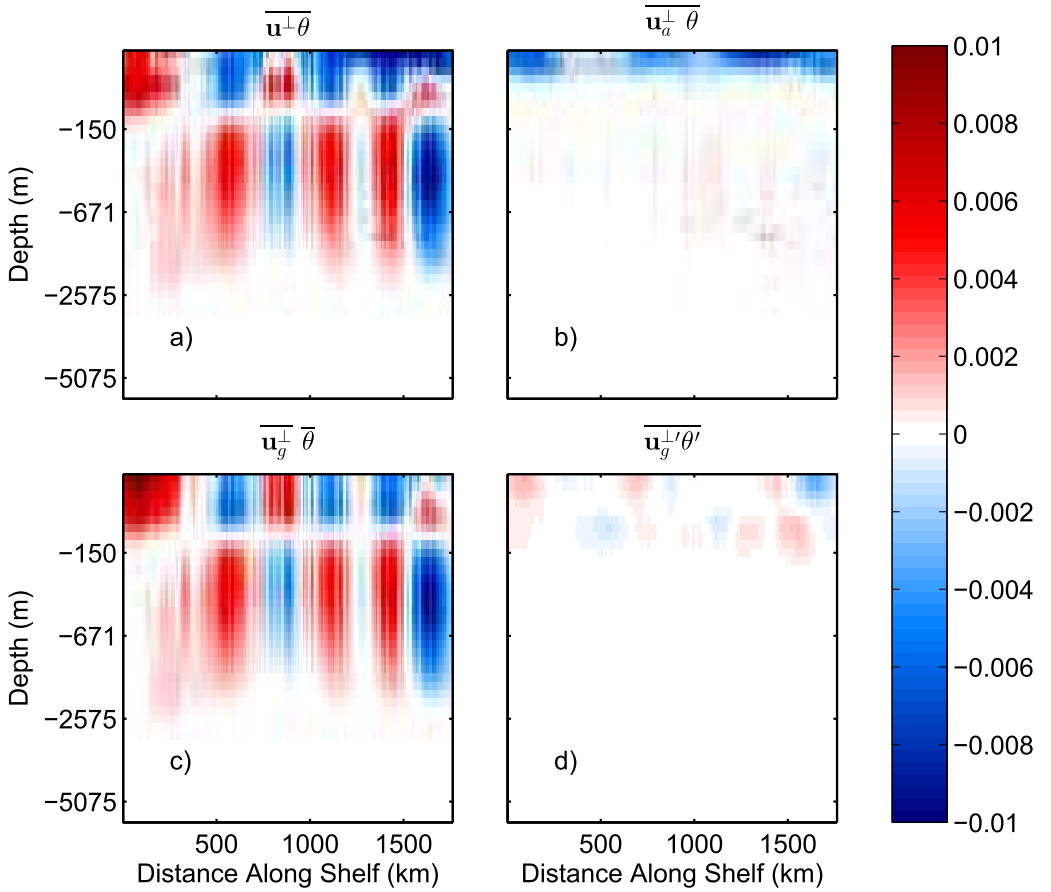

Figure 6. Temperature transports, in °C m s^{-1}, across the continental shelf given by equation (2), smoothed with a ~160 km running mean. The along-shelf distance is pictured by the red contour in Figure 1a from west to east. (a) Total time-mean transport. (b) Total ageostrophic component of the total time-mean transport. (c) Time-mean geostrophic component of the total time-mean transport. (d) Geostrophic eddy transport.

6. The Total Vorticity Budget

In order to identify the dominant mechanism driving the time-mean cross-shelf transport shown in Figure 6, we assess the full SOSE vorticity budget along the continental shelf slope. The vorticity tendency is

$$\underbrace{\zeta_t}_{\text{tendency}} + \underbrace{\beta v}_{\text{mean transport}} - \underbrace{\nabla\times\frac{\tau}{\rho}}_{\text{wind forcing}} - \underbrace{fw_z}_{\text{stretching}} + \underbrace{\nabla\times(\mathbf{u}\cdot\nabla\mathbf{u})}_{\text{advection}} - \underbrace{\nabla\times(\mathbf{V})}_{\text{viscosity}} = 0. \tag{3}$$

A derivation and description of this equation is given in Appendix A. Cross sections of the time-mean vorticity budget terms as a function of along continental shelf distance are shown in Figure 7. The time-mean total vorticity tendency is negligible compared to the other terms in equation (3). The meridional transport term, βv, provides the dominant contribution to cross-shelf heat transport when the shelf is zonally oriented, as is primarily the case in the Amundsen Sea. In most regions, the continental shelf slope serves as a barrier to flow penetrating the shelf region due to vorticity constraints. Here, however, this is not the case. Figure 6 shows temperature transport normal to the shelf-slope to be strong in many regions along the length of the ASE.

The cross sections shown in Figure 7 depict noisy regions near the ocean floor extending into the water column, where the balance is complex. Here the on-shelf flow (βv) reduces to a minimal value, and bottom boundary layer theory may more appropriately describe the dynamics. Figure 7e shows the along-shelf integral of the terms in equation (3) vertically integrated from the surface to 1904 m depth and divided by $\beta\times 10^6$ so that the units are that of volume transport in Sverdrups. Negative values indicate southward transport, i.e., toward the ASE. From this line plot, it is clear that the net transport is primarily negative, as is the

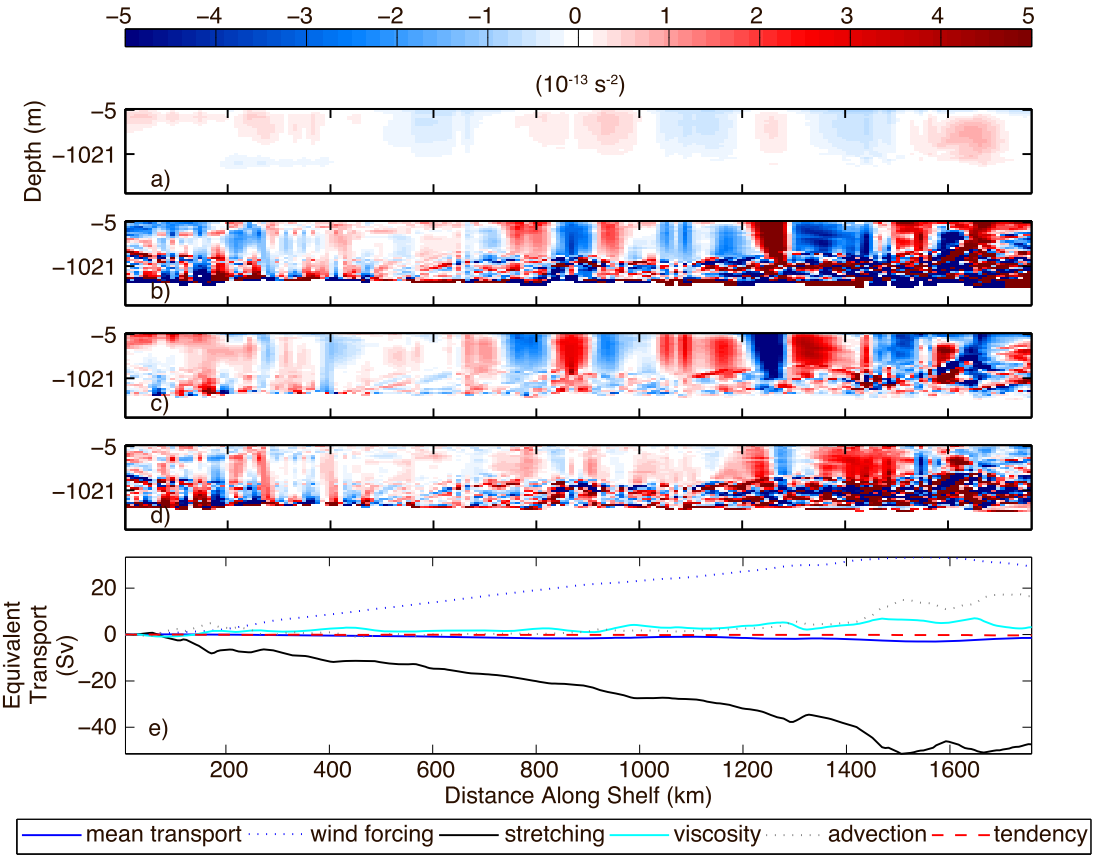

Figure 7. Time-mean vorticity budget, in $\times 10^{-13}$ s^{-2}, along the continental shelf given by equation (3). The along-shelf distance is pictured by the red contour in Figure 1a from west to east. (a) Mean transport: βv. (b) Wind forcing + stretching: $-\nabla\times(\tau/\rho)-fw_z$. (c) Advection: $\nabla\times(\mathbf{u}\cdot\nabla\mathbf{u})$. d) Viscosity: $-\nabla\times(\mathbf{V})$. e) Vertically integrated terms as a cumulative integral along the shelf slope, divided by $\beta\times 10^6$, giving units of transport (Sv).

stretching term, while the wind-stress curl, nonlinear advection, and viscous terms are primarily positive, balancing the vorticity budget to give 0.31 Sv total tendency over the 6 year mean. The 6 year mean balance integrated along the shelf is

$$(\beta\times 10^6)^{-1}\left(\zeta_t+\beta v-\nabla\times\frac{\tau}{\rho}-fw_z+\nabla\times(\mathbf{u}\cdot\nabla\mathbf{u})-\nabla\times(\mathbf{V})\right)=0$$

$$-0.31\ \text{Sv}-1.50\ \text{Sv}+29.34\ \text{Sv}-47.35\ \text{Sv}+16.64\ \text{Sv}+3.18\ \text{Sv}=0.$$

Thus, wind forcing, $-\nabla\times(\tau/\rho)$, along with non-linear and viscous terms, are primarily balanced by water column stretching, $-fw_z$. The residual sustains a time-mean meridional flow, βv, across the shelf slope. Stretching strongly counteracts on-shelf flow, but the input of vorticity from the wind-stress curl, augmented by interactions with open ocean currents, is enough to drive a ~1 Sv flow into the ASE from the open ocean.

7. Summary and Discussion

Ice mass loss from the WAIS outlet glaciers along the Amundsen Sea coastline has been attributed to basal melting forced by CDW found on the ASE continental shelf [*Walker et al.*, 2007; *Jenkins et al.*, 2010; *Pritchard et al.*, 2012; *Wåhlin et al.*, 2013]. Changing oceanic circulation may play a significant role in delivering heat to the grounding zone of the ASE outlet glaciers [*Holland et al.*, 2008]. We have used a state estimate of the Southern Ocean to identify a heat transport pathway to the ASE. Though we do not attempt to describe the circulation that occurs on the continental shelf in detail, we do identify a physical mechanism that delivers CDW to the shelf slope where it crosses into the embayment. In the Amundsen Sea region, the southern branch of the Antarctic Circumpolar Current system veers southeastward with a transport of over 1 Sv just

north of the shelf break (Figure 1b). Relatively warm CDW crosses the steep continental shelf into the ASE at several places along the shelf, with a consistently positive integrated temperature transport throughout 2005–2010. We find that heat is transported across the shelf at all depths. Our primary focus, however, is on the warm CDW found at depths below the permanent pycnocline ($\gamma^n \geq 28$ kg m^{-3}), as these waters are of the density class most likely to have direct bearing on basal melting. On the ASE shelf, the permanent pycnocline in SOSE is found at about 225 m. Below this depth, the ASE heat budget is dominated by the divergence of heat advection across the ASE boundaries, while diffusion acts to cool the shelf waters to a lesser extent. The result that heat diffusion across the permanent pycnocline is small should be taken with caution until observations can confirm or refute this hypothesis. Below 225 m depth, heat primarily enters the ASE from across the continental shelf break, exiting along the coast across the longitudinal boundaries of our ASE study region, 124.25°W and 98.42°W.

Previous studies have concurred that there is an oceanic heat transport pathway to the ASE [*Assmann et al*., 2013; *Martinson and McKee*, 2012; *Stewart and Thompson*, 2015; *St-Laurent et al*., 2013; *Walker et al*., 2013]. However, there has been no consensus as to what dynamics govern this pathway. There are many possible mechanisms including upwelling facilitated through surface Ekman transport, eddies, tides, and frictional processes [*Thoma et al*., 2008; *Assmann et al*., 2013; *Robertson*, 2013; *Walker et al*., 2013; *Stewart and Thompson*, 2015]. Here we have posed the hypothesis that there is a large-scale advective pathway of heat from the open ocean to the ASE. To address this, we diagnose the dynamical budgets in a model of the entire Southern Ocean that is consistent with available observations. We find a cross-shelf heat transport that is primarily geostrophic below the permanent pycnocline. The SOSE vorticity balance indicates that cross-shelf transport is driven by the local wind-stress curl, which is a dynamically relevant quantity that has previously been overlooked in favor of wind-stress [*Thoma et al*., 2008; *Spence et al*., 2014; *Schmidtko et al*., 2014]. The large-scale wind-stress curl forcing that we have identified is not the only mechanism at play. Future work must diagnose the relative importance of this large-scale pathway to the other mechanisms. Furthermore, the interplay of the dynamics at different scales needs to be addressed, including how the system responds to extreme or sustained wind changes.

While no study has explicitly examined vorticity dynamics driven by wind-stress curl in this region, the importance has been alluded to in other studies [e.g., *Dutrieux et al*., 2014; *Thoma et al*., 2008; *Wåhlin et al*., 2013], supporting our hypothesis. *Thoma et al*. [2008] find that temporal variability of cross-shelf CDW transport is related to wind forcing over the shelf break. Though vorticity constraints are not identified within their proposed possible transport mechanisms, the evidence for such a pathway presented here is not inconsistent with the model results of *Thoma et al*. [2008]. During their observational period, *Dutrieux et al*. [2014] found decreased glacial melt rates due to a depression of the thermocline forced by a weakened wind-stress curl over the shelf break. Additionally, the pseudo wind-stress correlation maps calculated by *Wåhlin et al*. [2013], exhibit a spatial structure characteristic of a system controlled by wind-stress curl, with correlations to the zonal wind that are positive to the south and negative to the north and correlations to the meridional wind that are positive to the east and negative to the west.

The realism of the reanalysis winds in this topographically complex region has only been validated by the few intermittent mean sea-level pressure measurements available in the near-by Bellingshausen Sea [*Bracegirdle*, 2012]. Further verification with long-term in situ wind measurements in the Amundsen Sea would be useful. Westerly winds over the Amundsen Sea have been shown to correlate strongly with the El Niño Southern Oscillation (ENSO) (Niño 3.4) during spring, and to a lesser extent, with the Southern Annular Mode (SAM) during the summer on decadal time-scales [*Bracegirdle*, 2012; *Steig et al*., 2012], while on multi-decadal scales, the North Atlantic Oscillation (NAO) is the more important driver of atmospheric variability in the Amundsen Sea [*Li et al*., 2014]. Future work must now determine how the local wind-stress curl over the Amundsen Sea Embayment, and consequently the input of vorticity into the ocean system, is sensitive to changes in modes of large-scale atmospheric variability such as SAM, ENSO, and the NAO.

Appendix A: Vorticity Budget Derivation

Ocean circulation generally follows contours of constant f/h, where f is the Coriolis parameter and h is the water column height. However, flow from the open ocean across the Amundsen Sea shelf decreases h and increases f, defying this general concept. This change in f/h necessitates either an increase in relative vorticity, which we do not find, or vorticity forcing through local time-mean wind-stress curl [*Sverdrup*, 1947].

The vorticity balance stands in contrast to the momentum balance, which provides a natural framework for evaluating the geostrophic currents that balance the pressure gradient term. The vorticity balance provides a means to evaluate deviations from the geostrophic balance that are associated with the curvature of the wind stress. In this context, we are primarily interested in the southward flow onto the ASE continental shelf, which is explicitly isolated in this equation. In the presence of strong bottom flows or steep topography, one must also consider the vorticity forcing induced from frictional boundary layers and pressure torques [*Hughes and de Cuevas*, 2001; *Spence et al*., 2012].

The full SOSE vorticity budget is:

$$\zeta_t + \nabla \cdot (f\mathbf{u}) + \nabla \times (\mathbf{u} \cdot \nabla \mathbf{u}) = \nabla \times \left(\frac{\tau}{\rho} + \mathbf{V} \right), \tag{A1}$$

where $\mathbf{u}$ is the horizontal velocity vector, τ is wind-stress, and $\mathbf{V}$ is the parameterized viscous term. Utilizing the nondivergent flow constraint $(\nabla \cdot \mathbf{u} = 0)$, allows isolation of the meridional flow in the planetary advection term:

$$\nabla \cdot (f\mathbf{u}) = (fu)_x - (-fv)_y = -fw_z + \beta v, \tag{A2}$$

where $\beta = f_y$. Due to the model discretization on a spherical grid, the pressure term does not vanish. In consistency with the model pressure solver formulation, we have added this contribution to the divergence term, and thus, it appears as a stretching term, $-fw_z$, in the vorticity budget.

Substituting 5 into 4 and rearranging, we find the following vorticity balance

$$\underbrace{\zeta_t}_{\text{tendency}} + \underbrace{\beta v}_{\text{mean transport}} - \underbrace{\nabla \times \frac{\tau}{\rho}}_{\text{wind forcing}} - \underbrace{fw_z}_{\text{stretching}} + \underbrace{\nabla \times (\mathbf{u} \cdot \nabla \mathbf{u})}_{\text{advection}} - \underbrace{\nabla \times (\mathbf{V})}_{\text{viscosity}} = 0. \tag{A3}$$

Acknowledgments

This work was supported by the National Science Foundation (NSF) Office of Polar Programs (grant ANT0961218), NSF Division of Ocean Sciences (grant OCE-1234473), NSF Scripps Institution of Oceanography Research Experience for Undergraduates (grant 1062305), and the National Oceanic and Atmospheric Administration (grant NA10OAR4310139). Computational resources for the SOSE were provided by NSF XSEDE resource grant OCE130007. The SOSE solution for the years 2005–2010, denoted iteration 100, is available from sose.ucsd.edu. The observations used for model validation are available from the NOAA National Ocean Data Center (http://www.nodc.noaa.gov/). The authors would like to thank Anna Wåhlin, as well as an additional reviewer for their helpful comments and suggestions on an earlier submission of this manuscript.

References

Assmann, K., A. Jenkins, D. Shoosmith, D. Walker, S. Jacobs, and K. Nicholls (2013), Variability of circumpolar deep water transport onto the Amundsen Sea continental shelf through a shelf break trough, *J. Geophys. Res. Oceans*, *118*, 6603–6620, doi:10.1002/2013JC008871.

Bamber, J. L., R. E. M. Riva, B. L. A. Vermeersen, and A. M. LeBrocq (2009), Reassessment of the potential sea-level rise from a collapse of the West Antarctic Ice Sheet, *Science*, *342*, 901–903.

Bracegirdle, T. J. (2012), Climatology and recent increase of westerly winds over the Amundsen Sea derived from six reanalyses, *Int. J. Climatol.*, *33*, 843–851.

Dutrieux, P., J. De Rydt, A. Jenkins, P. R. Holland, H. K. Ha, S. H. Lee, E. J. Steig, Q. Ding, E. P. Abrahamsen, and M. Schröder (2014), Strong sensitivity of Pine Island ice-shelf melting to climatic variability, *Science*, *343*(6167), 174–178.

Fenty, I., and P. Heimbach (2013), Coupled sea ice–ocean-state estimation in the Labrador Sea and Baffin Bay, *J. Phys. Oceanogr.*, *43*, 884–904.

Forget, G. (2010), Mapping ocean observations in a dynamical framework: A 2004-06 ocean atlas, *J. Phys. Oceanogr.*, *40*, 1201–1221.

Heimbach, P., and M. Losch (2012), Adjoint sensitivities of sub-ice-shelf melt rates to ocean circulation under the Pine Island Ice Shelf, West Antarctica, *Ann. Glaciol.*, *53*, 59–69.

Hibler, W. D., and K. Bryan (1987), A diagnostic ice–ocean model, *J. Phys. Oceanogr.*, *17*, 987–1015.

Holland, P. R., A. Jenkins, and D. M. Holland (2008), The response of ice shelf basal melting to variations in ocean temperature, *J. Clim.*, *21*, 2558–2572.

Hughes, C. W., and B. A. de Cuevas (2001), Why western boundary currents in realistic oceans are inviscid: A link between form stress and bottom pressure torques, *J. Phys. Oceanogr.*, *31*, 2871–2885.

Jacobs, S. S., A. Jenkins, G. F. Giulivi, and P. Dutrieux (2011), Stronger ocean circulation and increased melting under Pine Island Glacier ice shelf, *Nat. Geosci.*, *4*, 519–523.

Jenkins, A., P. Dutrieux, S. S. Jacobs, S. D. McPhail, J. R. Perrett, A. T. Webb, and D. White (2010), Observations beneath Pine Island Glacier in West Antarctica and implications for its retreat, *Nat. Geosci.*, *3*, 468–472.

Joughin, I., and R. B. Alley (2011), Stability of the West Antarctic Ice sheet in a warming world, *Nat. Geosci.*, *4*, 506–513.

Joughin, I., B. E. Smith, and B. Medley (2014), Marine ice sheet collapse potentially under way for the Thwaites Glacier Basin, West Antarctica, *Science*, *344*(6185), 735–738.

Large, W. G., J. C. McWilliams, and S. Doney (1994), Oceanic vertical mixing: A review and a model with a nonlocal boundary layer parameterization, *Rev. Geophys.*, *32*, 363–403.

Li, X., D. M. Holland, E. P. Gerber, and C. Yoo (2014), Impacts of the north and tropical Atlantic Ocean on the Antarctic Peninsula and sea ice, *Nature*, *505*, 538–542.

Losch, M., D. Menemenlis, J.-M. Campin, P. Heimbach, and C. Hill (2010), On the formulation of sea-ice models. Part 1: Effects of different solver implementations and parameterizations, *Ocean Modell.*, *33*, 129–144.

Martinson, D. G., and D. C. McKee (2012), Transport of warm Upper Circumpolar Deep Water onto the western Antarctic Peninsula continental shelf, *Nature*, *8*, 433–442.

Mazloff, M., P. Heimbach, and C. Wunsch (2010), An eddy-permitting Southern Ocean state estimate, *J. Phys. Oceanogr.*, *40*, 880–899.

Mouginot, J., E. Rignot, and B. Scheuchl (2014), Sustained increase in ice discharge from the Amundsen Sea Embayment, West Antarctica, from 1973 to 2013, *Geophys. Res. Lett.*, *41*, 1576–1584, doi:10.1002/2013GL059069.

Nøst, O., M. Biuw, V. Tverberg, C. Lydersen, T. Hattermann, Q. Zhou, L. Smedsrud, and K. Kovacs (2011), Eddy overturning of the Antarctic Slope Front controls glacial melting in the Eastern Weddell Sea, *J. Geophys. Res.*, *116*, C11014, doi:10.1029/2011JC006965.
Oppenheimer, M. (1998), Global warming and the stability of the West Antarctic Ice Sheet, *Nature*, *393*, 325–332.
Payne, A. J., A. Vieli, A. P. Shepherd, D. J. Wingham, and E. Rignot (2004), Recent dramatic thinning of the largest West Antarctic ice stream triggered by oceans, *Geophys. Res. Lett.*, *31*, L23401, doi:10.1029/2004GL02128.
Pritchard, H. D., S. R. M. Ligtenberg, H. A. Fricker, D. G. Vaughan, M. R. van den Broeke, and L. Padman (2012), Antarctic ice-sheet loss driven by basal melting of ice shelves, *Nature*, *484*, 502–505.
Rignot, E., J. L. Bamber, M. R. van den Broeke, C. Davis, Y. Li, W. J. van de Berg, and E. van Meijgaard (2008), Recent Antarctic ice mass loss from radar interferometry and regional climate modelling, *Nat. Geosci.*, *1*, 106–110.
Rignot, E., S. Jacobs, J. Mouginot, and B. Scheuchl (2013), Ice-shelf melting around Antarctica, *Science*, *341*, 266–270.
Rignot, E., J. Mouginot, M. Morlighem, H. Seroussi, and B. Scheuchl (2014), Widespread, rapid grounding line retreat of Pine Island, Thwaites, Smith, and Kohler glaciers, West Antarctica, from 1992 to 2011, *Geophys. Res. Lett.*, *41*, 3502–3509, doi:10.1002/2014GL060140.
Robertson, R. (2013), Tidally induced increases in melting of Amundsen Sea ice shelves, *J. Geophys. Res. Oceans*, *118*, 3138–3145, doi:10.1002/jgrc.20236.
Schmidtko, S., K. J. Heywood, A. F. Thompson, and S. Aoki (2014), Multidecadal warming of Antarctic waters, *Science*, *346*(6214), 1227–1231.
Schodlok, M. P., D. Menemenlis, E. Rignot, and M. Studinger (2012), Sensitivity of the ice-shelf/ocean system to the sub-ice-shelf cavity shape measured by NASA IceBridge in Pine Island Glacier, West Antarctica, *Ann. Glaciol.*, *53*, 156–162.
Semtner, A. J. (1976), A model for the thermodynamic growth of sea ice in numerical investigations of climate, *J. Phys. Oceanogr.*, *6*, 379–389.
Spence, P., O. A. Saenko, W. Sijp, and M. England (2012), The role of bottom pressure torques on the interior pathways of North Atlantic Deep Water, *J. Phys. Oceanogr.*, *42*, 110–125.
Spence, P., S. M. Griffies, M. H. England, A. M. Hogg, O. A. Saenko, and N. C. Jourdain (2014), Rapid subsurface warming and circulation changes of Antarctic coastal waters by poleward shifting winds, *Geophys. Res. Lett.*, *41*, 4601–4610, doi:10.1002/2014GL060613.
St-Laurent, P., J. M. Klinck, and M. S. Dinniman (2013), On the role of coastal troughs in the circulation of warm Circumpolar Deep Water on Antarctic shelves, *J. Phys. Oceanogr.*, *43*(1), 51–64.
Steig, E. J., Q. Ding, D. S. Battisti, and A. Jenkins (2012), Tropical forcing of Circumpolar Deep Water Inflow and outlet glacier thinning in the Amundsen Sea Embayment, West Antarctica, *Ann. Glaciol.*, *53*, 19–28.
Stewart, A. L., and A. F. Thompson (2015), Eddy-mediated transport of warm Circumpolar Deep Water across the Antarctic Shelf Break, *Geophys. Res. Lett.*, *42*, 432–440, doi:10.1002/2014GL062281.
Sverdrup, H. U. (1947), Wind-driven currents in a baroclinic ocean; with application to the equatorial currents of the Eastern Pacific, *Proc. Natl. Acad. Sci. U. S. A.*, *33*, 318–326.
Thoma, M., A. Jenkins, D. Holland, and S. Jacobs (2008), Modelling Circumpolar Deep Water intrusions on the Amundsen Sea continental shelf, Antarctica, *Geophys. Res. Lett.*, *35*, L18602, doi:10.1029/2008GL034939.
Thompson, A. F., K. J. Heywood, S. Schmidtko, and A. L. Stewart (2014), Eddy transport as a key component of the Antarctic overturning circulation, *Nat. Geosci.*, *7*(12), 879–884.
Venaille, A., G. K. Vallis, and K. S. Smith (2011), Baroclinic turbulence in the ocean: Analysis with primitive equation and quasigeostrophic simulations, *J. Phys. Oceanogr.*, *41*(9), 1605–1623.
Wåhlin, A. K., X. Yuan, G. Björk, and C. Nohr (2010), Inflow of Warm Circumpolar Deep Water in the Central Amundsen Shelf, *J. Phys. Oceanogr.*, *40*, 1427–1434.
Wåhlin, A., O. Kalén, L. Arneborg, G. Björk, G. Carvajal, H. Ha, T. Kim, S. Lee, J. Lee, and C. Stranne (2013), Variability of warm deep water inflow in a submarine trough on the Amundsen Sea Shelf, *J. Phys. Oceanogr.*, *43*, 2054–2070.
Walker, D. P., M. A. Brandon, A. Jenkins, J. T. Allen, J. A. Dowdswell, and J. Evans (2007), Ocean heat transport onto the Amundsen Sea shelf through a submarine glacial trough, *Geophys. Res. Lett.*, *34*, L02602, doi:10.1029/2006GL028154.
Walker, D. P., A. Jenkins, K. M. Assmann, D. R. Shoosmith, and M. A. Brandon (2013), Oceanographic observations at the shelf break of the Amundsen sea, Antarctica, *J. Geophys. Res. Oceans*, *118*, 2906–2918, doi:10.1002/jgrc.20212.
Warren, B. A. (1999), Approximating the energy transport across oceanic sections, *J. Geophys. Res.*, *104*, 7915–7919.
Whitworth, T., A. Orsi, S.-J. Kim, W. Nowlin, and R. Locarnini (1998), Water Masses and Mixing Near the Antarctic Slope Front, in *Ocean, Ice, and Atmosphere: Interactions at the Antarctic Continental Margin*, edited by S. S. Jacobs, and R. F. Weiss, AGU, Washington, D. C., doi:10.1029/AR075p0001.
Zhang, J., and W. Hibler III (1997), On an efficient numerical method for modeling sea ice dynamics, *J. Geophys. Res.*, *102*, 8691–8702.